

Pulsars Do Not Produce Sharp Features in the Cosmic-Ray Electron and Positron Spectra

Isabelle John^{1,*} and Tim Linden^{1,†}

¹Stockholm University and The Oskar Klein Centre for Cosmoparticle Physics, Alba Nova, 10691 Stockholm, Sweden

Pulsars are considered to be the leading explanation for the excess in cosmic-ray positrons detected by PAMELA and AMS-02. A notable feature of standard pulsar models is the sharp spectral cutoff produced by the increasingly efficient cooling of very-high-energy electrons by synchrotron and inverse-Compton processes. This spectral break has been employed to: (1) constrain the age of pulsars that contribute to the excess, (2) argue that a large number of pulsars must significantly contribute to the positron flux, and (3) argue that spectral cutoffs cannot distinguish between dark matter and pulsar models. We prove that this spectral feature does not exist — it appears due to approximations that treat inverse-Compton scattering as a continuous, instead of as a discrete and catastrophic, energy-loss process. Astrophysical sources do not produce sharp spectral features via cooling, reopening the possibility that such a feature would provide incontrovertible evidence for dark matter.

Observations by PAMELA [1] and AMS-02 [2–4] have provided clear evidence for a rise in the positron fraction at energies above ~ 10 GeV. This excess has most commonly been interpreted as either evidence of dark matter (e.g., [5]) or the production of electron and positron pairs (e^\pm , hereafter, electrons) by energetic pulsars [6, 7]. Over the last five years, TeV halo observations have shown that pulsars efficiently convert a large fraction of their spin-down power into energetic electrons, providing credence to the pulsar explanation [8–10].

In addition to energetic arguments, the positron spectrum has long been discussed (even before PAMELA) as a discriminant of the underlying mechanism. Dark matter models generically include sharp spectral “lines” at an energy corresponding to the dark matter mass [11]. However, pulsar models include their own sharp spectral feature located at an energy determined by the pulsar age and the energy-loss rate of very high-energy electrons [12]. These features are similar, and models for the PAMELA and AMS-02 data have discussed the difficulty in using spectral features to constrain their dark matter or pulsar origin [13–16], a topic which was revived after DAMPE observations [17] of a potential 1.4 TeV electron spectral bump [18–22].

As γ -ray data have begun to prefer the pulsar interpretation [8, 10, 23], recent studies have focused on whether the excess is dominated by a few nearby pulsars or a large ensemble of systems [6–8, 16, 24]. Spectral considerations again play an important role. Models predict that every pulsar will produce a spectral cutoff at an energy corresponding to the pulsar age. The detectability of this feature depends on its fractional contribution to the positron flux. Because AMS-02 does not find any sharp spectral features, models tend to prefer scenarios where many pulsars contribute to the excess [25–29].

The reason for this spectral feature is straightforward. Young pulsars spin down quickly, injecting most of their electrons in a few thousand years. These electrons cool rapidly through synchrotron and inverse-Compton scattering (ICS). Critically, both processes cool electrons at a rate that is proportional to the square of the electron energy. Thus, the highest energy electrons all cool to almost the same critical en-

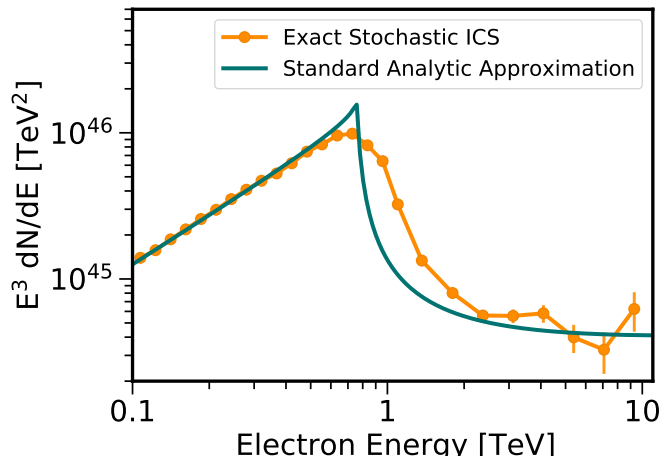


FIG. 1. The total electron spectrum integrated over all distances from a 370 kyr old pulsar (e.g., Geminga), obtained by the standard analytic approximation (blue), compared to our exact stochastic ICS model (orange). The sharp spectral feature at ~ 0.76 TeV is washed out, while the low and high energy behavior remains the same. Error bars are statistical due to the low-number of high-energy counts.

ergy regardless of their initial energy. Because the electrons are born at about the same time and travel through the same magnetic and interstellar radiation fields, they bunch up at a specific energy, above which there is a sharp cutoff.

However, this explanation depends on an incorrect simplification. It assumes that ICS is a continuous process where numerous interactions each remove infinitesimal energy from the electron. Instead, the ICS of high-energy electrons is a catastrophic process, where individual interactions remove a large fraction (~ 10 –100%) of the electron energy.

In this *letter*, we prove that when the stochasticity of ICS is correctly modeled, pulsars do not produce a sharp feature in the local cosmic-ray spectrum. Using a detailed Monte Carlo, we find that ICS energy losses typically produce a distribution of electron energies that are dispersed by $\sim 50\%$ around the standard “critical value”, washing out the sharp spectral effect (see Figure 1). Importantly, this result does not apply to dark matter models, where the spectral feature is instead directly produced in the annihilation event. Thus, our results have significant implications for our ability to differentiate dark matter and pulsar contributions to the positron flux.

* isabelle.john@fysik.su.se, ORCID: orcid.org/0000-0003-2550-7038

† linden@fysik.su.se, ORCID: orcid.org/0000-0001-9888-0971

Standard Pulsar Models. — Most pulsar studies use similar approaches. In App. A we recap these studies, and discuss small differences that do not affect our result. Here, we review *three* key conceptual points that are relevant for our results.

The *first* point is that most electrons are accelerated when the pulsar is young. High-energy emission is powered by the efficient conversion of a pulsar’s rotational kinetic energy into the acceleration of electron pairs, with a luminosity given by:

$$L(t) = \eta L_0 \left(1 + \frac{t}{\tau}\right)^{-2} \quad (1)$$

where L_0 is the initial luminosity, η is a (usually constant) conversion efficiency, and τ is a critical timescale, which theory and data both determine to be $\mathcal{O}(10)$ kyr. This is short compared to the timescale for electrons to diffuse to Earth, meaning that pulsars inject most of their power in a brief burst.

The *second* point is that the electron injection spectrum is hard and continues to very high energies. Standard models use an injection spectrum:

$$\frac{dN}{dE} = Q(t) E^{-\alpha} e^{-E/E_{cut}} \quad (2)$$

where $Q(t)$ is a normalization related to $L(t)$. Best-fit values for α span 1.5 – 2.2 [8, 9, 30], with E_{cut} between 0.01–1 PeV, though see Refs. [31, 32] for more detailed injection histories. This means that a large fraction of the electron power is injected at energies far above the GeV-scales where the local electron flux is best-measured.

The *third* point is that the energy-loss rate for high-energy electrons gets faster at higher energies, with a form:

$$\frac{dE}{dt} = -\frac{4}{3} \sigma_T c \left(\frac{E}{m_e}\right)^2 \left[\rho_B + \sum_i \rho_i(\nu_i) S(E, \nu_i) \right] \quad (3)$$

where σ_T is the Thomson cross section, E and m_e are the electron energy and mass, ρ_B is the magnetic field energy density, and ρ_i are the energy densities of interstellar radiation field (ISRF) components with photon energies ν_i . $S_i(E, \nu_i)$ accounts for the Klein-Nishina suppression of the ICS cross-section for very-high-energy electrons [33].

For magnetic fields of $B \sim 3 \mu\text{G} = 0.22 \text{ eV cm}^{-3}$, and ISRF strengths of 1 eV cm^{-3} , the energy-loss timescale is:

$$t_{loss} \approx 320 \text{ kyr} \left(\frac{E}{1 \text{ TeV}}\right)^{-1} \left(\frac{\rho_{\text{tot}} S_{\text{eff}}(E)}{1 \text{ eV cm}^{-3}}\right) \quad (4)$$

where S_{eff} is calculated by convolving the effect of Klein-Nishina suppression for each ISRF component. From this, we see that 1 TeV electrons require ~ 300 kyr to cool, while 100 TeV electrons require only ~ 3 kyr.

Finally, these terms are integrated into a diffusion equation, which determines the electron flux that propagates from a pulsar formed at $r=0$ and time $t=0$ to Earth at time corresponding to the pulsar age. Several different approaches are used, but the details are irrelevant to our results.

Eqns. (1 – 4) show how pulsars produce a spectral feature. The pulsar produces very-high-energy electrons in a δ -function-like burst. The most energetic electrons cool more quickly than lower-energy electrons, producing a spectrum that “bunches up” at a critical energy, E_c . This critical energy decreases with pulsar age, but is between 100–1000 GeV for the most important pulsars. This result is generic to any pulsar model that uses Eqn. (3) to calculate ICS cooling.

The Stochasticity of Inverse-Compton Scattering. — The problem with this approach stems from Eqn. (3), which calculates the *average* energy that an electron loses over a period of time, but does not account for the *dispersion* in these losses. Eqn. (3) treats energy losses as continuous, when they, in fact, stem from a finite number of interactions between an electron and ambient magnetic and radiation fields.

For synchrotron radiation, the difference is negligible. The critical energy for synchrotron radiation is given by:

$$\nu_c = \frac{3\gamma^2 e B}{4\pi m_e c} = 0.06 \left(\frac{B}{1 \mu\text{G}}\right) \left(\frac{E}{1 \text{ TeV}}\right)^2 \text{ eV} \quad (5)$$

Thus, the energy loss from each interaction is small, as is the relative variance in the number of interactions ($1/\sqrt{n}$).

For ICS, however, individual interactions are important. The ICS differential cross-section was originally computed in Ref. [33], and is reported here from Ref [34]:

$$\frac{d^2\phi(E_\gamma, \theta)}{d\Omega dE_\gamma} = \frac{r_0^2}{2\nu_i E^2} \times \left[1 + \frac{z^2}{2(1-z)} - \frac{2z}{b_\theta(1-z)} + \frac{2z^2}{b_\theta^2(1-z)^2} \right] \quad (6)$$

where E_γ is the final γ -ray energy, ν_i and E are the initial energies of the photon and electron and θ is the angle between them, and r_0 is the classical electron radius. The parameter $z \equiv E_\gamma/E$ and $b_\theta \equiv 2(1-\cos\theta)\nu_i E$. At low energies (Thomson regime), only the first term is non-zero, the cross-section is $\sigma_T = 6.6 \times 10^{-25} \text{ cm}^2$, and the relevant energy scales for this process are approximately:

$$E_{\gamma,c} = \frac{4}{3} \gamma^2 \nu_i \quad (7)$$

At high energies (Klein-Nishina regime) the critical energy surpasses the initial electron energy (which is not kinematically allowed), causing the cross-section to become suppressed and the typical γ -ray energy to become very peaked just below the electron energy.

Thus, even for scatterings with typical CMB photons ($\nu_i \sim 10^{-3} \text{ eV}$), a 1 TeV electron loses 5 GeV, a 10 TeV electron loses 500 GeV, and a 100 TeV electron loses 50 TeV. Energy losses for infrared ($\nu_i \sim 10^{-2} \text{ eV}$), optical ($\nu_i \sim 1 \text{ eV}$), and UV ($\nu_i \sim 10 \text{ eV}$), are even higher, and can fall well into the Klein-Nishina range.

Interstellar Radiation Field Model. — We model the interstellar radiation field (ISRF) based on four components: the cosmic-microwave background (energy density $u = 0.26 \text{ eV/cm}^3$, temperature $T = 2.7 \text{ K}$), infrared ($u = 0.60 \text{ eV/cm}^3$, $T = 20 \text{ K}$), optical ($u = 0.60 \text{ eV/cm}^3$, $T = 5000 \text{ K}$) and ultra-violet ($u = 0.10 \text{ eV/cm}^3$, $T = 20000 \text{ K}$) [8]. From this, we compute the photon number density in 18000 bins spanning from $10^{-5} - 10^3 \text{ eV}$ following a blackbody spectrum, and use Monte Carlo techniques to select target photons from this distribution.

Geminga as a Template System. — In our default analysis, we choose model parameters that are consistent with the best-fit values for Geminga, a nearby ($\sim 250 \text{ pc}$), middle-aged ($\sim 370 \text{ kyr}$) pulsar [35]. We assume an electron injection spectral index $\alpha = 1.9$ and energy cutoff $E_{\text{cut}} = 100 \text{ TeV}$ [8], normalized to the total energy output of Geminga $E_{\text{tot}} \approx 9.8 \times 10^{50} \text{ GeV}$, and an efficiency of converting spindown power into e^\pm pairs of $\eta = 0.1$. We adopt a time-dependent luminosity according to Eqn. (1), with a spin-down timescale of 9.1 kyr [8], *i.e.*, most of the total electron flux is injected in the first few thousand years after pulsar formation. We note that this last parameter may vary significantly between pulsars [21, 28]. As the pulsar ages and loses its rotational energy fewer electrons are produced. These early electrons are most important for producing the sharp cutoff in the electron spectrum.

Numerical Setup. — We utilize a Monte Carlo approach to account for the variance of ICS energy losses for individual electrons. The electron energy is calculated explicitly in time, as follows: (1) we begin with an electron formed at a time t after pulsar formation and an initial energy E_0 , (2) we evolve the system in time, choosing a time step small enough that both synchrotron losses and the probability of having two ICS interactions in a single time step are negligible, (3) based on the electron energy and photon density, we randomly determine whether an ICS interaction happens in the time step or not, and if so calculate the initial and final photon energy, (4) we re-compute the electron energy and repeat this process until the current age of the pulsar is reached.

To produce an accurate stochastic model, we inject $\sim 30,000$ electrons with an initial energy distribution following Eqn. 2 and time-distribution according to Eqn. 1. We include electrons with initial energies from 100 GeV to 1000 TeV with 5000 logarithmic bins. Because the number of electrons at high energies is rapidly falling, we create a dedicated dataset of $\sim 60,000$ electrons with initial energies above 1 TeV, and normalize it accordingly. To obtain the differential electron flux dN/dE as a function of electron energy, we bin the final electron energies into 35 logarithmic bins between 100 GeV and 10 TeV. For further illustrative parameter tests, we generate several datasets for electrons at specific initial energies, as described in the figures below and Appendix B.

We compare our stochastic method to an analytic calculation that results in the sharp spectral cutoff. For the analytic calculation, we use Equation A4, which gives the differential flux for an electron spectrum injected a time $t' = 370 \text{ kyr} - t$

ago for a pulsar at distance d from Earth with an injection spectrum following Equation 2 with 320 logarithmic bins between 100 GeV and 1000 TeV. To model the electron injection continuously over time, we sum the results for single delta-function injections for $t' = 0 - 370 \text{ kyr}$ and normalize the flux in each time step following Equation 1.

Only a small fraction of electrons produced by the pulsar reach Earth. Our stochastic model does not include diffusion and provides the total number of electrons produced by the pulsar. To compare our result with the analytic calculation, which gives the electron flux at radius r , we integrate the analytic flux over all space. We note that the average diffusion distance is given by $L_{\text{diff}} = \sqrt{6Dt}$. For a 1 TeV electron traveling for $t = 370 \text{ kyr}$ with a diffusion constant of $D_0 \sim 2 \times 28 \text{ cm}^2/\text{s}$ (see Eqn. (A6)), the typical electron diffusion distance is $L_{\text{diff}} \sim 1500 \text{ pc}$, which is larger than, but similar to the Earth distance. We stress that this approach does not affect our results, as the spectral feature depends on cooling, but not diffusion.

Results — Figure 2 shows the fundamental process that disperses the final electron energy. Starting with 4000 electrons at an initial energy of 10 TeV, we show the average energy lost per ICS interaction and the final electron energy at 370 kyr. On average, each ICS interaction removes $\sim 50 \text{ GeV}$ from an electron, indicating that stochastic variations in the number and strength of ICS events will lead to detectable dispersion in the electron energy. For these initial conditions, we calculate the dispersion to be $793 \pm 130 \text{ GeV}$.

Figure 3 shows the time-evolution of the electron energy shown in Figure 2 over 1 Myr. The initial dispersion in electron energies is small (owing to the fact that many electrons do not have any ICS interactions in the first few kyr). However, the dispersion increases at later times. At 1 Myr, the final electron energies are spread between 241 GeV and 331 GeV at 1σ and between 195 GeV and 377 GeV at 2σ . We note that the average final energy in our stochastic case is 286 GeV, which is slightly larger than the 264 GeV final energy in the standard analytic approximation, a fact which stems from the different treatments of Klein-Nishina suppression in our stochastic and analytic models.

Combining these features into a model for Geminga, we show our main result in Figure 1. The standard analytic approximation has three features: (1) a sharply rising electron spectrum at low energies, where the electrons are not cooled, and thus maintain their injection spectrum, (2) a steep drop at a critical energy that corresponds to the efficient cooling of higher-energy electrons that were produced near $t = 0$, and (3) a softer and dimmer high-energy spectrum produced by cooled electrons emitted at later times.

Our exact solution includes the first and third features, because the *average* ICS cooling is correct in the analytic approximation. However, the sharp spectral feature is smoothed out by the different energy losses experienced by individual electrons in the simulation. Notably, this effect is much larger than the energy resolution of current cosmic-ray experiments such as AMS-02, CALET and DAMPE [2, 17, 36], affecting the appearance of such a spectral feature in these instruments.

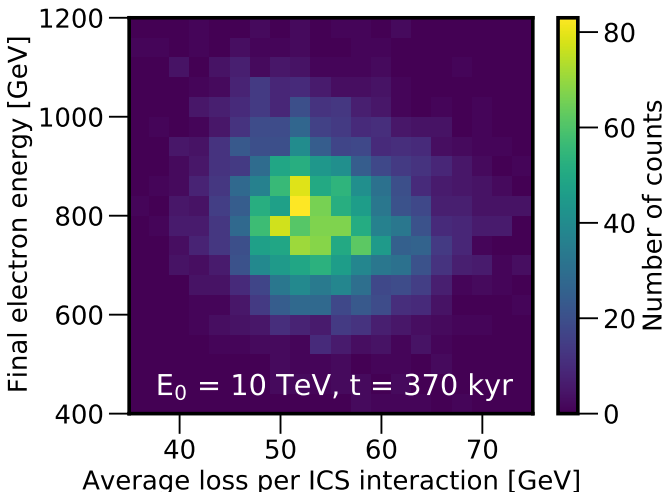


FIG. 2. The electron energy after 370 kyr compared to the average energy loss per ICS interaction. The dataset consists of 4000 electrons with an initial energy of 10 TeV. The significant energy loss per ICS interaction leads to a large dispersion in the final electron energy, preventing the formation of a spectral peak.

Discussion — We have shown that the standard analytic approximation for ICS cooling (Equation 3) induces an erroneous spectral feature in the local electron and positron fluxes. A proper treatment, which accounts for the stochasticity of ICS does not produce this feature. Physically, this stems from the fact that electrons in an ISRF only interact with a small random sample of the photon field, cooling to an energy that is only described by a probability distribution function rather than an exact value.

We stress that while this stochastic effect is most pronounced at high energies, it is not physically related to the kinematic effects of Klein-Nishina suppression, but is purely due to the statistics of ICS interactions. This fact is clearest in Figure 3, where we see that the significant dispersion in the final electron energies continues to nearly ~ 200 GeV, far lower than the standard Klein-Nishina range.

Our results are applicable to more diverse phenomena than pulsar models of the positron excess. ICS cooling cannot produce spectral features, owing to its inherent stochasticity. Our results hold for any system where particles are stochastically cooled, including *e.g.*, supernova models of the electron and positron fluxes in AMS-02 and DAMPE [20]. Similar effects, based on catastrophic energy loss processes, have also been noted in the case of $p\gamma$ interactions [37] and secondary antiproton production [38].

Interestingly, one could still observe a peaked local electron spectrum if cooling was dominated by synchrotron, rather than ICS losses — making a spectral peak a diagnostic for the energy loss process. However, for local studies, this is only an academic concern. Any source bright enough to contribute to the local electron flux, which also has sufficient local synchrotron cooling to dominate ICS losses throughout the ISRF would have already been detected in radio data.

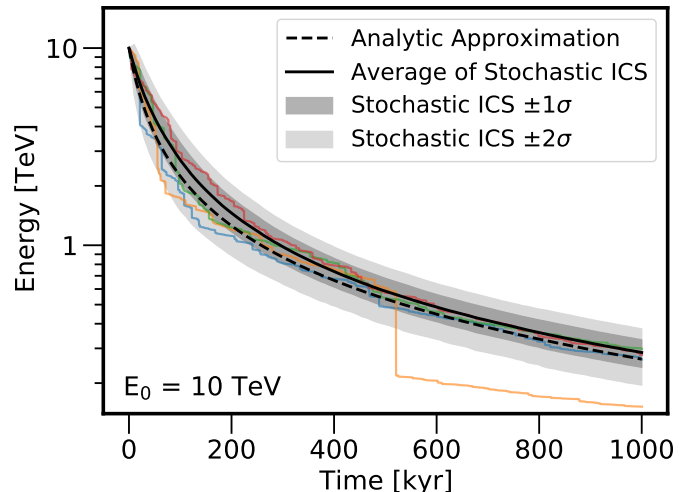


FIG. 3. The energy of an electron with an initial energy of 10 TeV over the 1 Myr duration of our simulation. The average (black solid line), and 1σ (dark gray) and 2σ (light gray) deviations are shown and compared with the electron energy from the analytic approximation. We show colored curves depicting a few typical events. We note that the analytic approximation and exact solution predict different average energies due primarily to differing treatments of Klein-Nishina suppression, which is not relevant to our result.

Effect on Pulsar Modeling — Our results have significant implications for pulsar models of the positron excess. Early studies realized that the number of pulsars that contribute to the excess is energy-dependent [6], due to the fact that the energy-dependence of the diffusion coefficient ($D \propto E^\delta$ with $\delta \sim 0.4$ [39]) is much weaker than the E^{-1} energy-loss timescale for synchrotron and ICS. This means that low-energy electrons can travel farther before cooling, and a larger population of pulsars can produce electrons that reach Earth. This was examined quantitatively in Ref. [29, 40], and our analysis does not affect this conclusion.

Recently, several studies have produced detailed models of Milky Way pulsars to determine the characteristics of systems that contribute to the positron flux [25, 27–29, 41]. Because these models produce χ^2 fits to AMS-02 (and sometimes DAMPE and CALET) data over a large energy range, they quantitatively constrain the presence of spectral features from individual pulsars. These constraints are significant because the observed electron and positron spectra are smooth. Generally, a wide variety of models can produce good fits to smooth power-law distributions, meaning that models that predict undetected spectral features can be strongly constrained.

We note that each of these models have many free parameters, and treat systematic errors differently. Thus, it is difficult to determine how the ICS approximation affects each. However, any model that uses an analytic ICS model will produce artificially strong constraints on the contribution from nearby pulsars with ages between ~ 100 –1000 kyr, because these systems would produce spectral features between 100–1000 GeV that have not been observed. This constraint is weaker at lower energies because a larger number of pulsars contributes to the excess, and weaker at higher energies because of the larger uncertainties in cosmic-ray data.

These constraints are in modest tension with TeV halo observations, which indicate that Geminga and Monogem (among others) are powerful electron accelerators. Studies have mentioned several effects that could be invoked in standard ICS models to decrease their spectral bumps, including: (1) anisotropies in energy-losses [13] or diffusion [42] that may affect the uniformity of the electron flux reaching Earth, (2) the effective trapping and cooling of young electrons within the pulsar wind nebulae [41, 43], (3) changes to the pulsar spin-down timescale which increase the fraction of electrons that are accelerated at late times [29], or (4) the energetic dominance by an extremely young pulsar with a spectral bump above the range of current constraints [28]. Our models do not necessarily reject such alternatives (several of which have physical justifications that extend beyond spectral arguments), but they do diminish the need for such models.

To be clear, our results show that pulsars do not produce sharp spectral features – a result which is based only on known particle physics. Our results re-open the possibility that only a small number of pulsars produce the positron excess at high-energies. Additionally, our analysis indicates that current (or even future [44]) studies of the electron and positron fluxes will not find sharp spectral features that can be used to constrain the age or proximity of nearby sources.

Effect on Dark Matter Searches — Dark matter particles that annihilate into e^\pm pairs or other hard leptonic states are predicted to produce features in the cosmic-ray positron spectrum, headlined by a sharp cutoff corresponding to the mass of the dark matter particle [11]. This spectral cutoff is intrinsic to the electron production process (and not caused by cooling). Our results do not affect this conclusion.

Excitingly, our analysis indicates that there is no standard astrophysical mechanism capable of producing a sharp feature in the local electron spectrum. The detection of such a feature, in this case, would serve as incontrovertible evidence of dark matter annihilation, or another novel physics process.

In fact, our results qualitatively point towards a slight enhancement of the dark matter spectral feature. In the analytic approximation, electrons observed just below the dark matter mass will have lost some energy due to a combination of synchrotron and ICS emission. However, many of these particles will, in fact, have undergone 0 ICS interactions, and will have an energy more closely concentrated near the dark matter mass than in the continuous case. This effect is quite small, but may enhance the detectability of such a feature with future telescopes like HERD [45] or AMS-100 [44].

Treatment of Diffusion — For clarity, this letter focuses on cooling and ignores diffusion. We quickly note that diffusion cannot “re-create” a spectral feature for two reasons: (1) the energy-dependence of diffusion is mostly monotonic. To create a spectral feature, the diffusion coefficient would need a sharp “spike” at a specific energy, (2) any diffusion-related spike would affect all cosmic rays at a specific rigidity, producing a sharp feature in all cosmic ray data that is ruled out by observations. We provide more details in Appendix D, and will produce a full model in an upcoming paper [46].

ACKNOWLEDGEMENTS

We thank Felix Aharonian, John Beacom, Ilias Cholis, Pedro De la Torre Luque, Carmelo Evoli, Ottavio Fornieri, Dan Hooper, Dmitry Khangulyan, Michael Korsmeier, Silvia Manconi, Igor Moskalenko, Payel Mukhopadhyay, Alberto Oliva, Luca Orusa, Stefano Profumo, Stefan Schael, Pasquale Serpico and Takahiro Sudoh for helpful comments. TL is supported by the Swedish National Space Agency under contract 117/19, the Swedish Research Council under contract 2019-05135 and the European Research Council under grant 742104. This project used computing resources from the Swedish National Infrastructure for Computing (SNIC) under project Nos. 2021/3-42, 2021/6-326 and 2021-1-24 partially funded by the Swedish Research Council through grant no. 2018-05973.

Appendix A: Cosmic-Ray Electron Acceleration and Propagation

The most common treatment of electron acceleration, propagation, and cooling in pulsars is as follows. The pulsar is born at time $t=0$ (matching the supernova) and immediately begins to inject e^+e^- pairs with a flux that is proportional to its spin-down power. The spin-down power is calculated using a simple model where the pulsar is treated as a mis-aligned rotating dipole, with a luminosity:

$$L(t) = \eta L_0 \left(1 + \frac{t}{\tau}\right)^{-(n+1)/(n-1)} \quad (\text{A1})$$

where L_0 is the power at time $t=0$ and is normalized to the pulsar kinetic energy, n is the breaking index, which is usually set to 3, η is an efficiency parameter, which is typically assumed to be constant with a typical range of 0.01–1 (though see [41, 43]), and τ sets the energy loss timescale, which can be calculated in the dipole model as:

$$\tau = \frac{3c^3 I P_0^2}{4\pi^2 B^2 R^6} \quad (\text{A2})$$

The specific value for τ can change significantly depending on the initial period and magnetic field strength of individual pulsars [21, 28, 47]. Here, we adopt $\tau = 9.1$ kyr, as calculated by Ref.[8] for the Geminga pulsar. Because this time scale is short compared to the ~ 100 kyr age of pulsars that contribute to the positron excess, some studies (e.g. Refs [7, 29]), further simplify the modeling by assuming that pulsars instantaneously inject all their energy at time $t = 0$.

The pulsar spectrum is typically modeled as a power-law with an exponential cutoff. However, the actual mechanism producing this acceleration is unclear, as there are two possibilities. The first is direct e^\pm pair production and acceleration at the pulsar magnetosphere, a process which may be either efficient or inefficient depending on the pulsar magnetosphere model, and which can continue to energies well-above 1 TeV [48, 49]. The second option is that the electrons are originally produced in the pulsar-magnetosphere, but are then re-accelerated (and their spectrum is reset) as they transit through the termination shock of the surrounding pulsar wind nebula [50–52]. Future observations of systems that do not include pulsar wind nebulae (e.g., millisecond-pulsars) could potentially distinguish these possibilities [53, 54].

In either case, the electron pairs diffuse away from the pulsar/pulsar wind nebula, following a process that is typically treated using the diffusion/convection equation of the form:

$$\frac{\partial}{\partial t} \frac{d\psi}{dE} (E, r, t) = \vec{\nabla} \cdot \left[D(E) \nabla \frac{d\psi}{dE} - v_c \frac{d\psi}{dE} \right] + \frac{d}{dE} \left[\frac{dE}{dt} \frac{d\psi}{dE} \right] + \delta(r) Q_0(r, t, E) \quad (\text{A3})$$

where $D(E)$ is the diffusion coefficient, which is typically normalized to fit cosmic-ray secondary-to-primary ratios,

with a typical energy dependence $D(E) \propto E^\alpha$ with α in the range 0.33 – 0.5 [39], v_c is a convection term which we will set to 0 in this study, the energy derivative accounts for energy losses due to synchrotron and ICS, and finally Q_0 is the source term, which is a spectrum-dependent normalization constant that is set such that the integral of the pulsar emission matches the pulsar luminosity from Eq. A1.

While this transport equation must typically be solved numerically, there is an commonly-employed analytic formula in the case that the cosmic-ray injection rate is a delta-function in time, which is given by:

$$\frac{dN}{dE} = \frac{Q(E)}{\pi^{3/2} d^3} (1 - bt'E)^{(\alpha-2)} \left(\frac{d}{D_{\text{diff}}} \right)^3 e^{-(d/D_{\text{diff}})^2} \quad (\text{A4})$$

where d is the distance from the pulsar to Earth, t' is the time since electron injection (e.g., 370 kyr - t) and D_{diff} is:

$$D_{\text{diff}}(E_e, t') \approx 2 \sqrt{D(E_e) t' \frac{1 - (1 - E_e/E_{\text{max}})^{1-\delta}}{(1-\delta) E_e/E_{\text{max}}}}. \quad (\text{A5})$$

E_{max} is the maximum energy that can be lost due to conversion of energy, given by $E_{\text{max}} \approx 1/(bt')$, and $D(E_e)$ is the diffusion coefficient for a specific electron energy given by:

$$D(E_e) = D_0 \times \left(\frac{E_e}{1 \text{ GeV}} \right)^\delta, \quad (\text{A6})$$

where we take $D_0 = 2 \times 10^{28} \text{ cm}^2/\text{s}$ at an electron energy of 1 GeV and a diffusion spectral index of $\delta = 0.4$.

Following Equation 3, the energy loss rate is typically written as a continuous process, which is given by:

$$\frac{dE}{dt} = -b(E) \times \left(\frac{E}{1 \text{ GeV}} \right)^2, \quad (\text{A7})$$

where b is typically calculated as:

$$b(E) = 1.02 \times 10^{-16} \times \left(\sum_i \frac{\rho_i}{\text{eV/cm}^3} S_i(E) + \rho_{\text{mag}} \left(\frac{B}{3 \mu\text{G}} \right)^2 \right) \text{ GeV/s.} \quad (\text{A8})$$

though we note that there are more accurate analytic prescriptions in the literature which take into account the energy-dependence of b [55]. In particular, this cross-section is inhibited at high-energies due to Klein-Nishina suppression, which decreases the incidence angles over which a photon and electron have a high-interaction probability. Studies have either used an exact calculation of the Klein-Nishina suppression [33], or utilized a simplified suppression factor first calculated in [56], which is given by:

$$S_i(E) \approx \frac{45m_e^2}{64\pi^2 T_i^2} \times \frac{1}{\frac{45m_e^2}{64\pi^2 T_i^2} + \frac{E^2}{m_e^2}}, \quad (\text{A9})$$

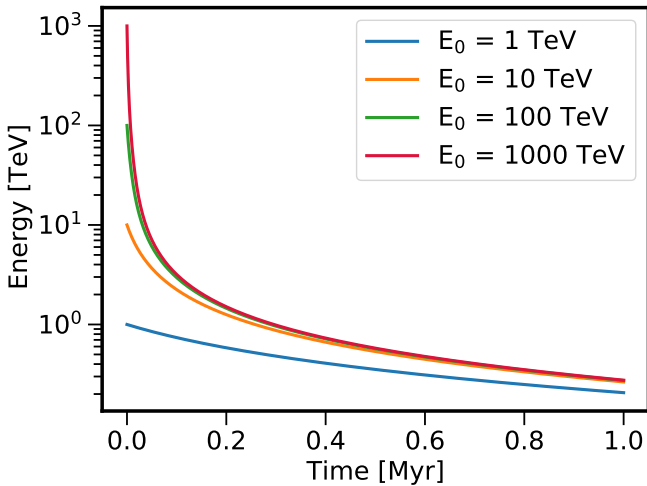


FIG. 4. The evolution of the electron energy over 1 Myr in the standard analytic approximation for electrons with different initial energies (1 TeV (blue), 10 TeV (orange), 100 TeV (green) and 1000 TeV (red)). Electrons with higher initial energies cool more rapidly than lower energy electrons, causing the electrons to cool down to similar energies over time, producing a spectral feature.

where E is the positron energy, m_e the positron mass and T_i the temperature of the respective ISRF component. Recent work has shown that the approximate solution is inadequate to deal with the high-precision of AMS-02 electron data in the GeV band [57, 58]. However, we stress that the difference between these approaches is not relevant for our study – because both are calculated within the continuous energy-loss formalism. Any method utilizing Equation 3 will incorrectly induce an electron spectral peak regardless of whether an incorrect or approximate model for the Klein-Nishina effect is employed.

The effect of ICS cooling depends sensitively on the model for the ISRF. There are many possibilities, including full spectral models based on multiwavelength observations as well as approximate models that bin the ISRF into a few major components with specified energies. In this study, we take the temperatures $T_{\text{UV}} = 20 \times 10^3$ K, $T_{\text{optical}} = 5 \times 10^3$ K, $T_{\text{IR}} = 20$ K and $T_{\text{CMB}} = 2.7$ K, and the energy densities $\rho_{\text{UV}} = 0.1$ eV/cm³, $\rho_{\text{optical}} = 0.6$ eV/cm³, $\rho_{\text{IR}} = 0.6$ eV/cm³, $\rho_{\text{CMB}} = 0.26$ eV/cm³, $\rho_{\text{mag}} = 0.224$ eV/cm³ (corresponding to a magnetic field strength of $B = 3$ μ G). [8]. We again stress that differences between these approaches are not responsible for the feature we identify in the main text.

Figure 4 shows the energy losses for the analytic approximation over 1 Myr for electrons with different initial energies. Electrons with high energies cool faster than electrons with low energies, and over time cool down to similar energies. After 1 Myr, the electrons with initial energies between 10 and 1000 TeV have roughly cooled to the same energy, 0.27 TeV. The fact that a larger fraction of initial lines converge at later times drives the fact that models of pulsar contributions provide increasingly peaky spectral features for older pulsars.

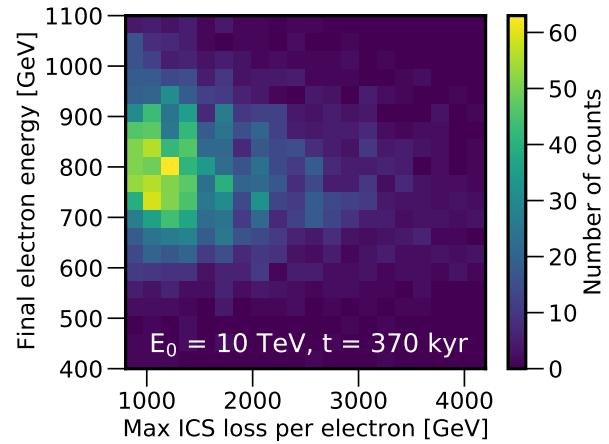


FIG. 5. The final electron energy compared to the maximum energy loss for an electron with an initial energy of 10 TeV that is cooled over 370 kyr. The vast majority of electrons have at least one ICS interaction which removes over 1 TeV from the electron.

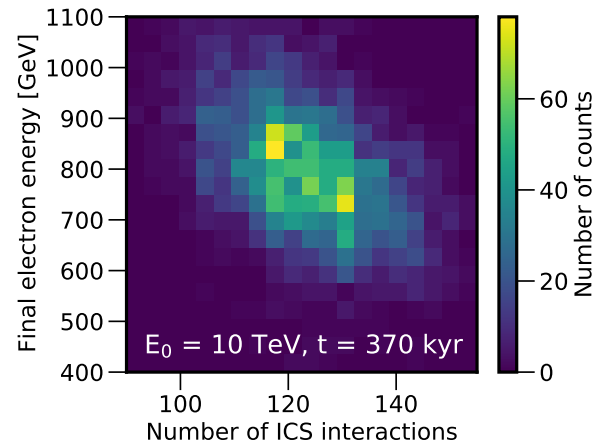


FIG. 6. The final electron energy compared to the number of ICS interactions an electron with initial energy 10 TeV experiences over 370 kyr.

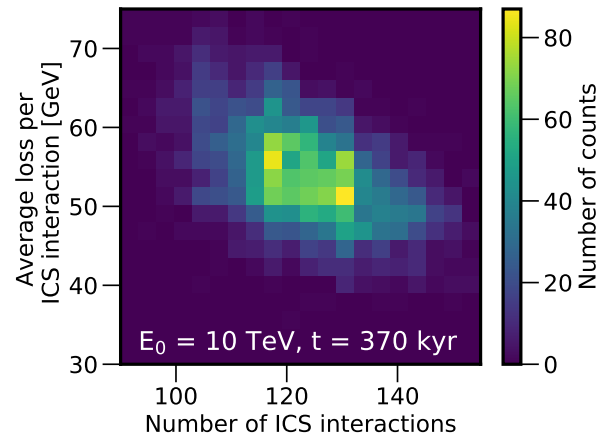


FIG. 7. The average energy loss per ICS interaction for an electron compared to the number of ICS interactions an electron with initial energy 10 TeV experiences over 370 kyr.

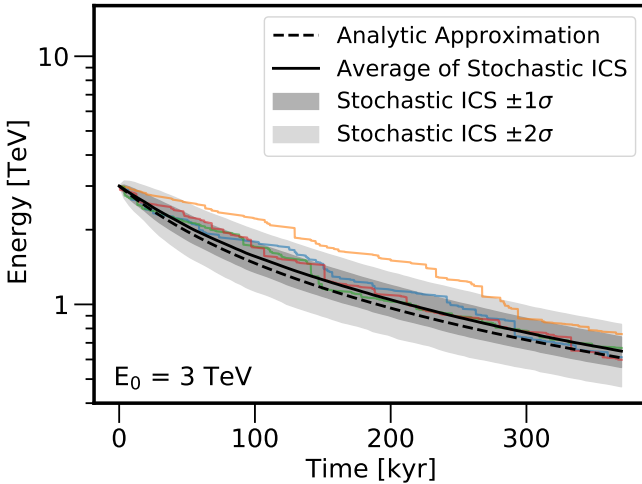


FIG. 8. The electron energy as a function of time for initial electron energy of 3 TeV. A similar dispersion is seen despite the lower starting energy.

Appendix B: Further Analysis of Stochastic Inverse-Compton Scattering

Figures 5–7 show further plots of the electrons used in Figures 2 and 3, for 1000 electrons with an initial energy of 10 TeV. In Figure 5, the final electron energy is shown compared to the maximum energy loss an electron has experienced in an ICS interaction. The maximum energy losses are around 800 to 1800 GeV, which is a significant fraction the total electron energy. Over 370 kyr, these electrons undergo relatively few ICS interactions, as can be seen in Figure 6, where the final electron energy is shown against the number of ICS interactions per electron. Typically, electrons undergo 100–140 interactions. The large spread in the energy loss per ICS interactions and the large variation in the number of interactions results in the large spread of final electron energies. Finally, Figure 7 shows the average energy loss per ICS interaction compared to the number of ICS interactions it undergoes.

Figure 8 shows the evolution of the electron energy over 370 kyr, similar to Figure 3, but with an initial electron energy of 3 TeV. The final average energy of the exact stochastic ICS calculation is 648 GeV (black-solid) with an energy spread of 557–740 GeV at 1σ and 466–831 GeV at 2σ . The final energy in the standard analytic approximation is 609 GeV (black-dotted). The colored lines represent the energy losses of a few individual electrons. The dataset contains 1000 electrons.

Appendix C: Isotropic Inverse-Compton Scattering

In many scenarios, the ISRF is isotropic, based on contributions from many optical and infrared sources. Thus, many studies use an isotropic version of the ICS cross-section, which is equivalent to Equation 6 integrated over solid angle:

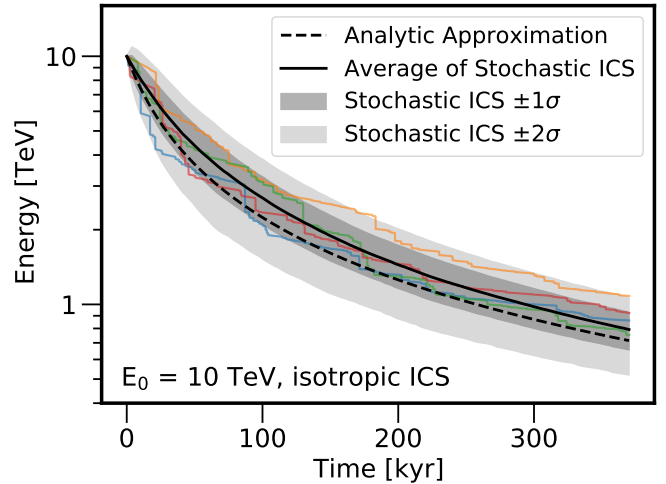


FIG. 9. The electron energy against time for initial electron energy of 10 TeV for the isotropic ICS calculation. The results are qualitatively the same.

$$\frac{dN(E_\gamma)}{dE_\gamma} = \frac{2\pi r_0^2}{\nu_i E^2} \times \left[1 + \frac{z^2}{2(1-z)} + \frac{z}{b(1-z)} - \frac{2z^2}{b^2(1-z)^2} - \frac{z^3}{2b(1-z)^2} - \frac{2z}{b(1-z)} \ln\left(\frac{b(1-z)}{z}\right) \right], \quad (C1)$$

where ν_i is the initial photon energy, E_γ the outgoing gamma energy, E the electron energy before the interaction, and $z \equiv E_\gamma/E$ and $b \equiv 4\nu_i E$.

Figure 9 shows the electron energy as a function of pulsar age for electrons produced at pulsar birth, 370 kyr ago, with an initial energy of 10 TeV for 1000 electrons. This is identical to Figure 3, but for an isotropic ICS calculation. The analytic ICS calculation is shown as a black-dashed line, while the average of the stochastic ICS is given as the black-solid line with the 1σ and 2σ bands in dark gray and light gray, respectively. The colored lines represent a few examples of individual electrons. The final energy in the exact stochastic ICS calculation is 792 GeV with an energy spread between 656–928 GeV at 1σ and 520–1065 GeV at 2σ , which is similar to the results of the non-isotropic case, as expected.

Appendix D: Treatment of Diffusion

Throughout the bulk of this paper, we have focused on the effect of electron cooling on the local electron spectrum generated by a nearby, middle-aged pulsar. However, the electrons produced by this source also must diffuse through the interstellar medium, and the treatment of particle diffusion may affect the electron spectrum observed at Earth.

However, diffusion does not affect the production of the sharp spectral feature in the analytic approximation. In Figure 10 we show the local electron flux produced by Geminga

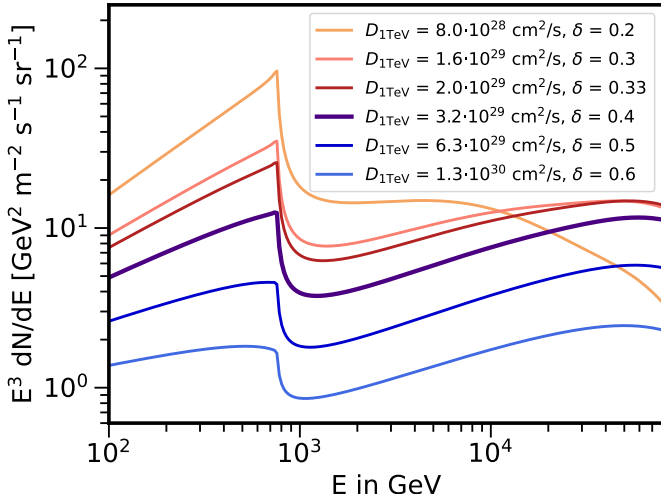


FIG. 10. The local electron flux observed at Earth calculated using the analytic approximation when diffusion is included. The distance and Results are shown for a number of diffusion indices and normalizations at a standard energy of 1 TeV. We note that both the location and sharpness of the spectral peak is not affected by the diffusion conditions, implying that it is generated by the cooling term, and is insensitive to particle diffusion.

using multiple different choices for the diffusion coefficient

(at 1 TeV) and the diffusion index. Because this changes the energy-dependent fraction of cosmic-rays that are near the Earth position after 370 kyr, it changes both the normalization and the overall spectrum of the electron flux both below and above the peak. However, the location and sharpness of the spectral feature is relatively unaffected, because it stems from the effective cooling of very-high-energy electrons.

We also stress that diffusion cannot “produce” a spectral feature that is similar to that observed in the analytic case. As shown in Figure 10, changes in the diffusion coefficient can either harden or soften the observed electron spectrum by producing energy-dependent changes in the fraction of the electron flux which is found at a specific distance from the initial source. However, the effect of diffusion is normally monotonic, as the increasing rigidity of high-energy particles makes them more capable of propagating through interstellar turbulence. In order to produce a spectral feature, the diffusion coefficient must have a significant local minimum or maximum, such that cosmic-rays at a specific energy are much more likely to be observed at a specific distance. Moreover, unlike in the case of particle cooling where the enhanced cooling rate becomes increasingly extreme at higher energies, any energy-dependent diffusion effect could not be boosted by increasing by coupling the effect across-different energies, or else the spectral effect would be extremely broad. Thus, there is no reasonable scenario in which diffusion itself can produce a sharp spectral feature in the electron data.

[1] O. Adriani, G. C. Barbarino, G. A. Bazilevskaya, R. Bellotti, M. Boezio, E. A. Bogomolov, L. Bonechi, M. Bongi, and PAMELA Collaboration, Phys. Rev. Lett. **105**, 121101 (2010), arXiv:1007.0821 [astro-ph.HE].

[2] AMS-02 Collaboration (AMS Collaboration), Phys. Rev. Lett. **113**, 121101 (2014).

[3] M. Aguilar *et al.* (AMS), Phys. Rev. Lett. **122**, 101101 (2019).

[4] M. Aguilar *et al.* (AMS), Phys. Rev. Lett. **122**, 041102 (2019).

[5] N. Arkani-Hamed, D. P. Finkbeiner, T. R. Slatyer, and N. Weiner, Phys. Rev. D **79**, 015014 (2009), arXiv:0810.0713 [hep-ph].

[6] D. Hooper, P. Blasi, and P. D. Serpico, JCAP **01**, 025 (2009), arXiv:0810.1527 [astro-ph].

[7] S. Profumo, Central Eur. J. Phys. **10**, 1 (2011), arXiv:0812.4457 [astro-ph].

[8] D. Hooper, I. Cholis, T. Linden, and K. Fang, Phys. Rev. D **96**, 103013 (2017), arXiv:1702.08436 [astro-ph.HE].

[9] A. U. Abeysekara *et al.* (HAWC), Science **358**, 911 (2017), arXiv:1711.06223 [astro-ph.HE].

[10] S. Profumo, J. Reynolds-Cordova, N. Kaaz, and M. Silverman, Phys. Rev. D **97**, 123008 (2018), arXiv:1803.09731 [astro-ph.HE].

[11] M. S. Turner and F. Wilczek, Phys. Rev. D **42**, 1001 (1990).

[12] F. A. Aharonian, A. M. Atoyan, and H. J. Voelk, A&A **294**, L41 (1995).

[13] D. Malyshev, I. Cholis, and J. Gelfand, Phys. Rev. D **80**, 063005 (2009), arXiv:0903.1310 [astro-ph.HE].

[14] V. Barger, Y. Gao, W. Y. Keung, D. Marfatia, and G. Shaughnessy, Phys. Lett. B **678**, 283 (2009), arXiv:0904.2001 [hep-ph].

[15] N. Kawanaka, K. Ioka, and M. M. Nojiri, ApJ **710**, 958 (2010), arXiv:0903.3782 [astro-ph.HE].

[16] T. Linden and S. Profumo, Astrophys. J. **772**, 18 (2013), arXiv:1304.1791 [astro-ph.HE].

[17] G. Ambrosi *et al.* (DAMPE), Nature **552**, 63 (2017), arXiv:1711.10981 [astro-ph.HE].

[18] B.-B. Wang, X.-J. Bi, S.-J. Lin, and P.-f. Yin, (2017), arXiv:1707.05664 [astro-ph.HE].

[19] K. Fang, X.-J. Bi, and P.-F. Yin, ApJ **854**, 57 (2018), arXiv:1711.10996 [astro-ph.HE].

[20] X.-J. Huang, Y.-L. Wu, W.-H. Zhang, and Y.-F. Zhou, Phys. Rev. D **97**, 091701 (2018), arXiv:1712.00005 [astro-ph.HE].

[21] O. Fornieri, D. Gaggero, and D. Grasso, JCAP **02**, 009 (2020), arXiv:1907.03696 [astro-ph.HE].

[22] Y. Bao, Y. Chen, and S. Liu, Mon. Not. Roy. Astron. Soc. **500**, 4573 (2020), arXiv:2010.12170 [astro-ph.HE].

[23] K. Fang, X.-J. Bi, P.-F. Yin, and Q. Yuan, Astrophys. J. **863**, 30 (2018), arXiv:1803.02640 [astro-ph.HE].

[24] I. Cholis and D. Hooper, Phys. Rev. D **88**, 023013 (2013), arXiv:1304.1840 [astro-ph.HE].

[25] I. Cholis, T. Karwal, and M. Kamionkowski, Phys. Rev. D **97**, 123011 (2018), arXiv:1712.00011 [astro-ph.HE].

[26] K. Fang, X.-J. Bi, and P.-f. Yin, Mon. Not. Roy. Astron. Soc. **478**, 5660 (2018), arXiv:1706.03745 [astro-ph.HE].

[27] I. Cholis, T. Karwal, and M. Kamionkowski, Phys. Rev. D **98**, 063008 (2018), arXiv:1807.05230 [astro-ph.HE].

[28] L. Orusa, S. Manconi, F. Donato, and M. Di Mauro, JCAP **12**, 014 (2021), arXiv:2107.06300 [astro-ph.HE].

[29] I. Cholis and I. Krommydas, Phys. Rev. D **105**, 023015 (2022), arXiv:2111.05864 [astro-ph.HE].

[30] M. Di Mauro, S. Manconi, and F. Donato, Phys. Rev. D **100**, 123015 (2019), [Erratum: Phys. Rev. D 104, 089903 (2021)], arXiv:1903.05647 [astro-ph.HE].

[31] D. Caprioli, P. Blasi, and E. Amato, Mon. Not. Roy. Astron. Soc. **396**, 2065 (2009), arXiv:0807.4259 [astro-ph].

[32] N. Bucciantini, Mon. Not. Roy. Astron. Soc. **480**, 5419 (2018), arXiv:1808.08757 [astro-ph.HE].

[33] G. R. Blumenthal and R. J. Gould, Rev. Mod. Phys. **42**, 237 (1970).

[34] F. A. Aharonian and A. M. Atoyan, Ap&SS **79**, 321 (1981).

[35] R. N. Manchester, G. B. Hobbs, A. Teoh, and M. Hobbs, Astron. J. **129**, 1993 (2005), arXiv:astro-ph/0412641.

[36] O. Adriani *et al.*, Phys. Rev. Lett. **120**, 261102 (2018), arXiv:1806.09728 [astro-ph.HE].

[37] F. A. Aharonian, B. L. Kanevskii, and V. V. Vardanian, Ap&SS **167**, 93 (1990).

[38] I. V. Moskalenko, A. W. Strong, J. F. Ormes, and M. S. Potgieter, Astrophys. J. **565**, 280 (2002), arXiv:astro-ph/0106567.

[39] M. Korsmeier and A. Cuoco, (2021), arXiv:2112.08381 [astro-ph.HE].

[40] O. M. Bitter and D. Hooper, (2022), arXiv:2205.05200 [astro-ph.HE].

[41] C. Evoli, E. Amato, P. Blasi, and R. Aloisio, Phys. Rev. D **103**, 083010 (2021), arXiv:2010.11955 [astro-ph.HE].

[42] A. Do, M. Duong, A. McDaniel, C. O'Connor, S. Profumo, J. Rafael, C. Sweeney, and W. Vera, III, Phys. Rev. D **104**, 123016 (2021), arXiv:2012.14507 [astro-ph.HE].

[43] Y. A. Gallant, Nuclear and Particle Physics Proceedings **297-299**, 106 (2018).

[44] S. Schael *et al.*, Nucl. Instrum. Meth. A **944**, 162561 (2019), arXiv:1907.04168 [astro-ph.IM].

[45] S. N. Zhang *et al.* (HERD), Proc. SPIE Int. Soc. Opt. Eng. **9144**, 91440X (2014), arXiv:1407.4866 [astro-ph.IM].

[46] I. John and T. Linden, (2022), 2208.XXXXX.

[47] T. Sudoh, T. Linden, and J. F. Beacom, Phys. Rev. D **100**, 043016 (2019), arXiv:1902.08203 [astro-ph.HE].

[48] A. A. Philippov and A. Spitkovsky, Astrophys. J. **855**, 94 (2018), arXiv:1707.04323 [astro-ph.HE].

[49] C. Kalapotharakos, G. Brambilla, A. Timokhin, A. K. Harding, and D. Kazanas, Astrophys. J. **857**, 44 (2018), arXiv:1710.03170 [astro-ph.HE].

[50] B. M. Gaensler and P. O. Slane, Ann. Rev. Astron. Astrophys. **44**, 17 (2006), arXiv:astro-ph/0601081.

[51] L. Sironi and A. Spitkovsky, ApJ **726**, 75 (2011), arXiv:1009.0024 [astro-ph.HE].

[52] B. Cerutti and G. Giacinti, Astron. Astrophys. **642**, A123 (2020), arXiv:2008.07253 [astro-ph.HE].

[53] D. Hooper and T. Linden, Phys. Rev. D **98**, 043005 (2018), arXiv:1803.08046 [astro-ph.HE].

[54] D. Hooper and T. Linden, Phys. Rev. D **105**, 103013 (2022), arXiv:2104.00014 [astro-ph.HE].

[55] D. Khangulyan, F. A. Aharonian, and S. R. Kelner, Astrophys. J. **783**, 100 (2014), arXiv:1310.7971 [astro-ph.HE].

[56] R. Schlickeiser and J. Ruppel, New Journal of Physics **12**, 033044 (2010), arXiv:0908.2183 [astro-ph.HE].

[57] M. Di Mauro, F. Donato, and S. Manconi, Phys. Rev. D **104**, 083012 (2021), arXiv:2010.13825 [astro-ph.HE].

[58] K. Fang, X.-J. Bi, S.-J. Lin, and Q. Yuan, Chin. Phys. Lett. **38**, 039801 (2021), arXiv:2007.15601 [astro-ph.HE].